ADVANCED MATERIALS
www.advmat.de

Coordination Chemistry as a Universal Strategy for a Controlled Perovskite Crystallization

Weiwei Zuo, Mahdi Malekshahi Byranvand, Tim Kodalle, Mohammadreza Zohdi, Jaekeun Lim, Brian Carlsen, Theresa Magorian Friedlmeier, Małgorzata Kot, Chittaranjan Das, Jan Ingo Flege, Wansheng Zong, Antonio Abate, Carolin M. Sutter-Fella, Meng Li, and Michael Saliba**

The most efficient and stable perovskite solar cells (PSCs) are made from a complex mixture of precursors. Typically, to then form a thin film, an extreme oversaturation of the perovskite precursor is initiated to trigger nucleation sites, e.g., by vacuum, an airstream, or a so-called antisolvent. Unfortunately, most oversaturation triggers do not expel the lingering (and highly coordinating) dimethyl sulfoxide (DMSO), which is used as a precursor solvent, from the thin films; this detrimentally affects long-term stability. In this work, (the green) dimethyl sulfide (DMS) is introduced as a novel nucleation trigger for perovskite films combining, uniquely, high coordination and high vapor pressure. This gives DMS a universal scope: DMS replaces other solvents by coordinating more strongly and removes itself once the film formation is finished. To demonstrate this novel coordination chemistry approach, $MAPbI_3$ PSCs are processed, typically dissolved in hard-to-remove (and green) DMSO achieving 21.6% efficiency, among the highest reported efficiencies for this system. To confirm the universality of the strategy, DMS is tested for $FAPbI_3$ as another composition, which shows higher efficiency of 23.5% compared to 20.9% for a device fabricated with chlorobenzene. This work provides a universal strategy to control perovskite crystallization using coordination chemistry, heralding the revival of perovskite compositions with pure DMSO.

1. Introduction

The power conversion efficiency (PCE) of perovskite solar cells (PSCs) with an ABX_3 structure—where A = Cs^+, methylammonium (MA^+), formamidinium (FA^+); B = Sn^{2+} or Pb^{2+}; X = Cl^-, Br^- or I^-—have sky-rocketed from 3.8%[1] in 2009 to now >25%.[2] To achieve higher thermal, moisture, and phase stabilities, we and others have designed various compositions based primarily on mixtures of $FAPbI_3$ with additives such as K^+, Rb^+, Br^-, Cl^-, SCN^-, and more.[3–6] Essentially, the purpose of this multicomponent engineering approach is to stabilize the photoactive "black phase" of $FAPbI_3$ at room temperature. This complexity, however, imposes challenges during film processing.[7]

At the same time, solvent engineering is equally important to manipulate the crystallization of perovskite films.[8] Currently, an antisolvent is used to supersaturate the perovskite precursor during

W. Zuo, M. M. Byranvand, M. Zohdi, J. Lim, C. Das, M. Saliba
Institute for Photovoltaics (*ipv*)
University of Stuttgart
Pfaffenwaldring 47, 70569 Stuttgart, Germany
E-mail: mahdi.malekshahi@ipv.uni-stuttgart.de;
michael.saliba@ipv.uni-stuttgart.de

M. M. Byranvand, C. Das, M. Saliba
Helmholtz Young Investigator Group FRONTRUNNER
IEK5-Photovoltaik
Forschungszentrum Jülich
52425 Jülich, Germany

The ORCID identification number(s) for the author(s) of this article can be found under https://doi.org/10.1002/adma.202302889

DOI: 10.1002/adma.202302889

T. Kodalle, C. M. Sutter-Fella
Molecular Foundry
Lawrence Berkeley National Laboratory
1 Cyclotron Road, Berkeley, CA 94720, USA

B. Carlsen
Laboratory of Photomolecular Science
École Polytechnique Fédérale de Lausanne
1015 Lausanne, Switzerland

T. Magorian Friedlmeier
Zentrum für Sonnenenergie- und Wasserstoff-Forschung
Baden-Württemberg (ZSW)
Meitnerstrasse 1, 70563 Stuttgart, Germany

M. Kot, J. I. Flege
Applied Physics and Semiconductor Spectroscopy, Brandenburg
University of Technology Cottbus-Senftenberg
Konrad-Zuse-Strasse 1, 03046 Cottbus, Germany

W. Zong
Organisch-Chemisches Institut
Ruprecht-Karls-Universität Heidelberg
Im Neuenheimer Feld 270, 69120 Heidelberg, Germany

the spin coating, e.g. chlorobenzene (CB), which is orthogonal on mixture *N,N*-dimethylformamide (DMF) and dimethyl sulfoxide (DMSO). Typically, a mixture of DMSO and DMF is used to dissolve multicomponent perovskites. The usage of the antisolvent is followed by nucleation during the subsequent annealing step.[9–14]

Additionally, the antisolvent is used rather naively since there is no or hard-to-predict coordination with the perovskite precursor components depending also on the exact composition used. For example, the all-inorganic $CsPbI_3$ coordinates while hybrid perovskites often do not.[15] Thus, the strongly coordinating DMSO often stays behind in the thin film.

Here, we demonstrate that coordination chemistry with respect to functional group and vapor pressure of solvents. This novel coordination chemistry is enabled by new sulfide-based green solvents such as dimethyl sulfide (DMS), which combines the highest yet reported donicity with among the highest vapor pressures reported in the literature. In addition, among the ether-type solvents, DMS is the one that is common in nature. Some ether solvents, such as tetrahydrofuran[16] and diethyl ether (DE),[17] are also frequently used in the study of perovskite, while we use DMS for the first time as an antisolvent, and compared this with diethyl sulfide (DES) and dipropyl sulfide (DPS) with various boiling points based on different carbon branched chain lengths of sulfur atoms to optimize perovskite crystallization. This opens a new door for perovskite research toward a controlled crystallization already at the early film formation stages.

2. Results and Discussion

The Gutmann D_N is a measure of the ability of a solvent to solvate cations and to react with Lewis acids based on coordination chemistry theory.[18,19] **Figure 1**A shows the Gutmann D_N and vapor pressure of DMSO, DMF, CB and DMS as the involved solvents in perovskite films fabrication (all the detailed parameters including D_N, dielectric constant, dipole moment and vapor pressure for all solvents are shown in Table S1, Supporting Information). Generally, solvents with high D_N coordinate strongly with the Pb^{2+} cations. Therefore, varying the concentration of high-D_N additives in precursor solutions tunes the Pb–solvent interactions.[20,21] Among the typical solvents for perovskite processing, DMS shows the highest D_N while maintaining a high vapor pressure.

At the same time, Figure 1A also shows that DMSO has a relatively high donor number and a low vapor pressure leading to significant challenges in extracting DMSO from the formed film. Current extraction solvents include CB, which has a low donor number and therefore does not coordinate with DMSO.

To highlight this point, we focus on $MAPbI_3$ in the following since it dissolved in pure DMSO unlike multicomponent perovskites that also use the more volatile DMF as the majority solvent for the precursor preparation. Moreover, the archetypical $MAPbI_3$ has advantages over multicomponent perovskites, such as a stable black phase at room temperature, less risk for phase segregation (only three components are needed), and an almost ideal bandgap at 1.58 eV.[6,7,22–27] While MA's volatility remains a challenge, reports show that appropriate encapsulation may be a possible remedy.[28,29]

One challenge with $MAPbI_3$ films is the instability against temperatures over 100 °C.[30] Thus, using DMSO (high coordination and a boiling point of 189 °C) with a very low vapor pressure nucleation trigger, such as CB, leads to a conflict between the perovskite degradation and the required temperature to degas the DMSO during the perovskite annealing (see Figure 1A).

To explore the performing mechanism of the solvents during the perovskite crystallization, we conduct Fourier-transform infrared (FTIR) spectroscopy for analyzing the intermediate phases and perovskite films (Figure 1B). The FTIR spectrum of pure DMSO is measured as the reference. The pure DMSO shows the S=O stretching peaks at 1400 cm^{-1},1309 cm^{-1}, and 1043 cm^{-1}, respectively. In the spectra of the perovskite intermediate phase obtained using CB and DMS, the S=O stretching peak at 1043 cm^{-1} is covered by the stretching peak signal of C–N at 1010 cm^{-1}, which then appears as a companion peak in the spectra, and in the annealed perovskite phase, this stretching peak disappears. The S=O stretching peak at 1400 cm^{-1} disappears only in the spectra of the perovskite phase with DMS as the coordination solvent, however, the stretching peak of S=O at 1309 cm^{-1} disappears in the spectra of the perovskite intermediate phase and the annealed black phase when DMS is used as the coordination solvent. This suggests that due to the high D_N and the mutual miscibility with DMSO,[31] DMS extract DMSO very efficiently and replaces its position in the MAI–PbI_2–DMSO adduct at the intermediate phase by coordinating its sulfur functional group to the Pb^{2+} cations. Afterward, DMS can leave the intermediate phase during the annealing process due to its high vapor pressure, leading to uniform nucleation and controlled crystallization. Based on these observations, we schematically illustrate the possible mechanism of DMS as a strong coordination solvent during the perovskite crystallization in Figure 1C. In addition, we investigated the initial adsorption energies of molecular DMS and DMSO using density functional theory to understand the interactions between DMS or DMSO and PbI2 (001) surfaces. Our results show that DMS forms intermediates more readily with PbI_2 than with DMSO (see Figure S1, Table S1, and Note S1, Supporting Information).

To get a more detailed understanding of the perovskite crystallization, we provide in situ film characterization. Figure 2 shows the evolution of the photoluminescence (PL) measured during spin-coating and annealing at 100 °C using CB and DMS,

A. Abate
Helmholtz-Zentrum Berlin für Materialien und Energie GmbH
Hahn-Meitner-Platz 1, 14109 Berlin, Germany
A. Abate
Department of Chemical
Materials and Production Engineering
University of Naples Federico II
pzz.le Vincenzo Tecchio 80, Naples 80125, Italy
M. Li
Key Lab for Special Functional Materials of Ministry of Education
National & Local Joint Engineering Research Center for High-efficiency Display and Lighting Technology
School of Materials Science and Engineering
Collaborative Innovation Center of Nano Functional Materials and Applications
Henan University
Kaifeng 475004, China

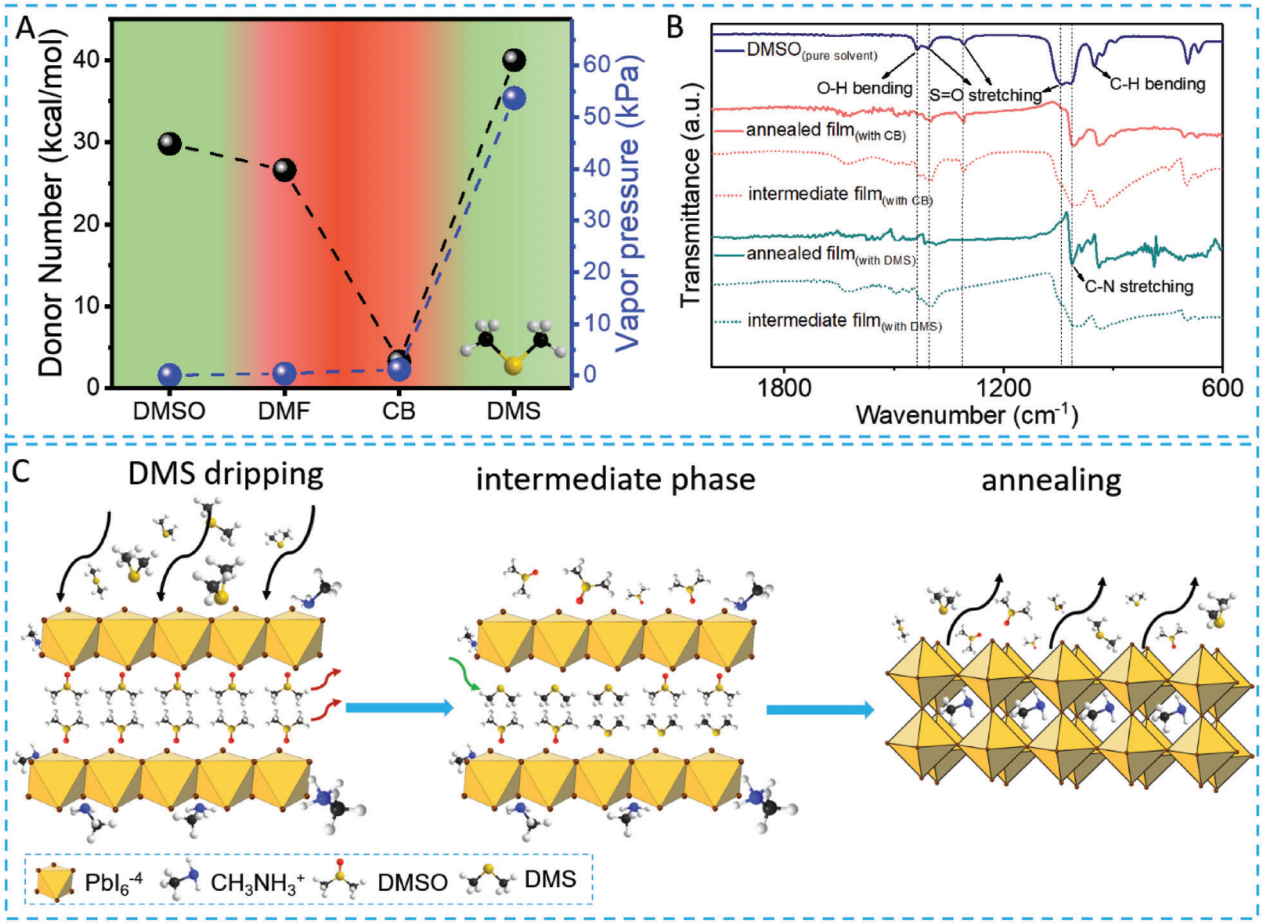

Figure 1. The mechanism of $MAPbI_3$ crystallization by assisting the solvent extraction role of DMS. A) Gutmann donor numbers and vapor pressure (at 20 °C) of different solvents including DMSO, DMF, CB, and DMS. B) FTIR spectra of pure DMSO, as well as of perovskite films deposited by CB and DMS before (intermediate phase) and after annealing. C) Schematic illustration of the proposed mechanism of DMS for perovskite crystallization.

respectively. Figure S2 (Supporting Information) shows the same evolution for deposited perovskite films by all four solvents. To elucidate the formation dynamics on a structural level, we show in situ grazing-incidence wide-angle X-ray scattering (GIWAXS) patterns of the CB sample in Figure S3A (Supporting Information). Due to the very low viscosity of DMS, we could not measure in situ GIWAXS on that corresponding sample. Instead, Figure S3B (Supporting Information) shows the GIWAXS evolution in the case of DES. Combining the PL and the GIWAXS data, we divide the film formation into three growth stages that will be discussed in the following. Comparing the PL-data of all five cases suggests that the perovskite growth follows similar dynamics via these three stages for all solvents.

In Stage I, after the initial solution ejection during the first ≈5 s of the spin-coating process, there is a weak PL signal emerging centered ≈1.58 eV. This signal is also present in the case of DMS but not visible in **Figure 2**B due to the different intensity-scaling of both panels (see color bars on the right side of Figure 2) – a differently scaled version of the same plot showing the existence of the weak PL-signal at 1.58 eV is shown in Figure S4 (Supporting Information). GIWAXS during the first stage only shows peaks associated with the ITO substrates which cannot explain the PL emission (see Figure S3, Supporting Information). Interestingly, the PL emission peak position coincides with the bandgap of $MAPbI_3$ but $MAPbI_3$ crystallization or formation is not expected and has not been reported before at this early stage and room temperature. Instead, during spin coating, before dripping the solvent, and depending on the exact precursor composition and solvent choice, solvate phases may form quickly.[32] We have shown before, that small volume inclusions of the perovskite phase may not show up in the diffraction pattern but PL is very sensitive to these bright emitting phases.[33] Other in situ PL studies during perovskite formation found blueshifted PL emission at the early crystallization stages explained by excitonic confinement in low dimensional perovskite structures.[34] Here, we can only speculate that the weak PL signal in Stage I may be attributed to an amorphous or intermediate, $MAPbI_3$-containing phase.

Upon the solvent drop, the beginning of Stage II, the initial PL-signal vanishes, and distinctive diffraction peaks appear (e.g., at 0.46 $Å^{-1}$, 0.51 $Å^{-1}$, and 0.65 $Å^{-1}$) that can be attributed to the orthogonal crystalline solvent complex, $Pb_3I_8.2(CH_3)_2SO.2CH_3NH_3$ ($MAPbI_3$·DMSO solvent complex).[42–44] In addition, dropping DMS or CB induces the occurrence of a very intense PL-peak centered at 1.64 and 1.7 eV, respectively, but is not present in the other cases at room temperature. Two possible explanations are considered to explain the

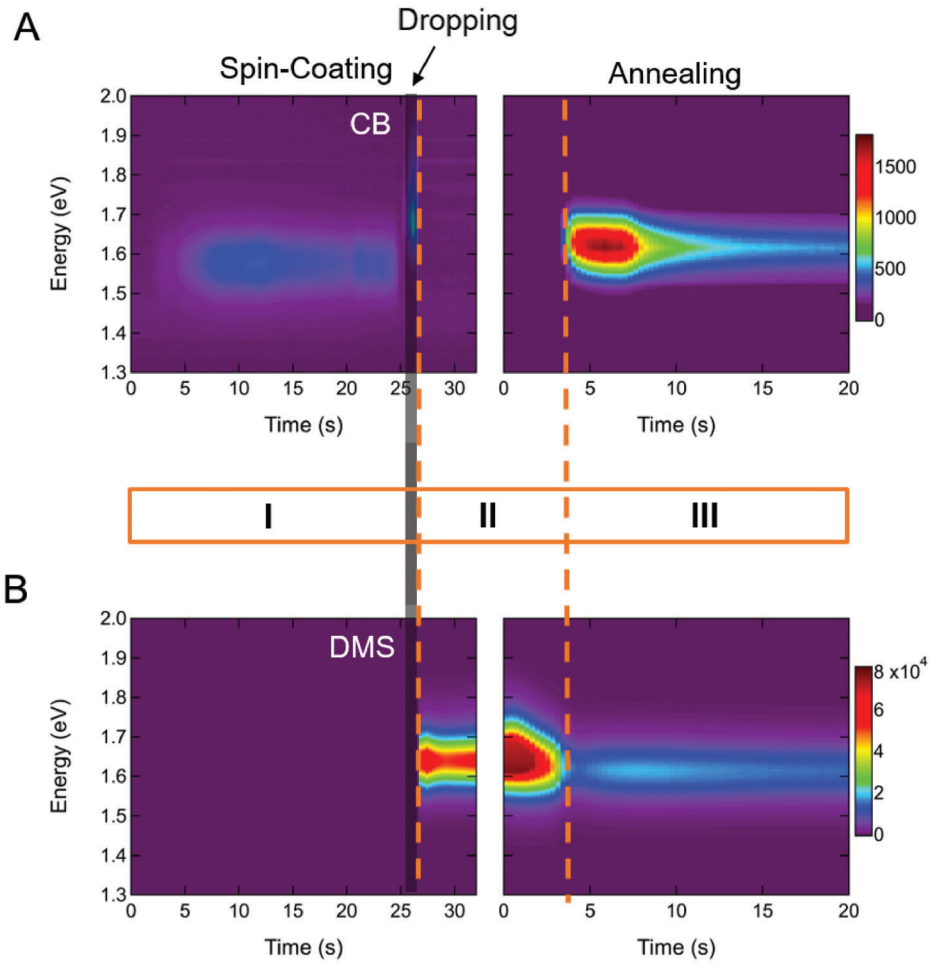

Figure 2. In situ characterization of perovskite films. A,B) The evolution of the photoluminescence signal during spin-coating (left column) and annealing (right column) of a $MAPbI_3$ sample deposited by assisting CB (A) and DMS (B). (The black arrow indicates the drop time point of the solvent).

PL emission energy higher than the bandgap energy. Dripping of DMS or CB likely leads to an exchange mechanism of DMS or CB with DMSO leading to the formation of a luminescent intermediate phase containing 2D-layered nanosheets or other low dimensional perovskite clusters.[34] In the case of CB and in analogy to a previous report,[33] we interpret the short PL "flash" in the case of CB as immediate $MAPbI_3$ nanocrystal formation. The PL is blueshifted compared to the bulk bandgap due to quantum confinement effects. The emergence of PL in the cases of DMS and CB but not for DPS and DES possibly indicates a different interaction with DMSO. For DMS and CB, DMSO is likely removed efficiently and locally during the dripping event while it is not as efficiently extracted with DPS and DES. In the case of CB, the quantum-confined perovskite nuclei formation appears metastable at this stage as large amounts of DMSO are still present in the wet film, hence the PL signal disappears very quickly. As the signal remains constant in the case of DMS, it appears that DMS is more efficiently extracting the DMSO, creating more stable nuclei. In addition, the short-lived PL signal appearing right after CB dripping is more blueshifted than the PL peak appearing after DMS dripping which indicates that nuclei are smaller in the case of CB.[35]

During annealing, i.e., in Stage III, the PL-emission of the DMS sample slightly redshifts before the appearance of the $MAPbI_3$-related PL-peak centered ≈1.61 eV (see Figure 2). The PL intensity drop and re-appearance of the $MAPbI_3$-related PL in the DMS case is likely caused by a second nucleation and growth event upon dissociation of the intermediate phase when reaching the final annealing temperature. With increasing annealing duration, this signal fades due to temperature-induced PL-quenching,[36] as well as degradation due to the constant laser-illumination. These dynamics are in good agreement with the GIWAXS data, which shows that the intermediate phase (in all investigated cases) undergoes thermal dissociation and subsequent solvent evaporation leading to the growth of $MAPbI_3$ and PbI_2 crystals (see Figures S3, Supporting Information).

Judging by the in situ PL and GIWAXS data, the choice of the solvent and consequently the solvent-solvent interaction, as well as the subsequent coordination chemistry do affect the formation dynamics of the final $MAPbI_3$ crystals during annealing. However, there are indications that DMS dripping is the most efficient in extracting DMSO, leads to larger initial nuclei, and a faster and more defined $MAPbI_3$ absorbance edge as measured by in situ transmission (see highlighted area in Figure S5,

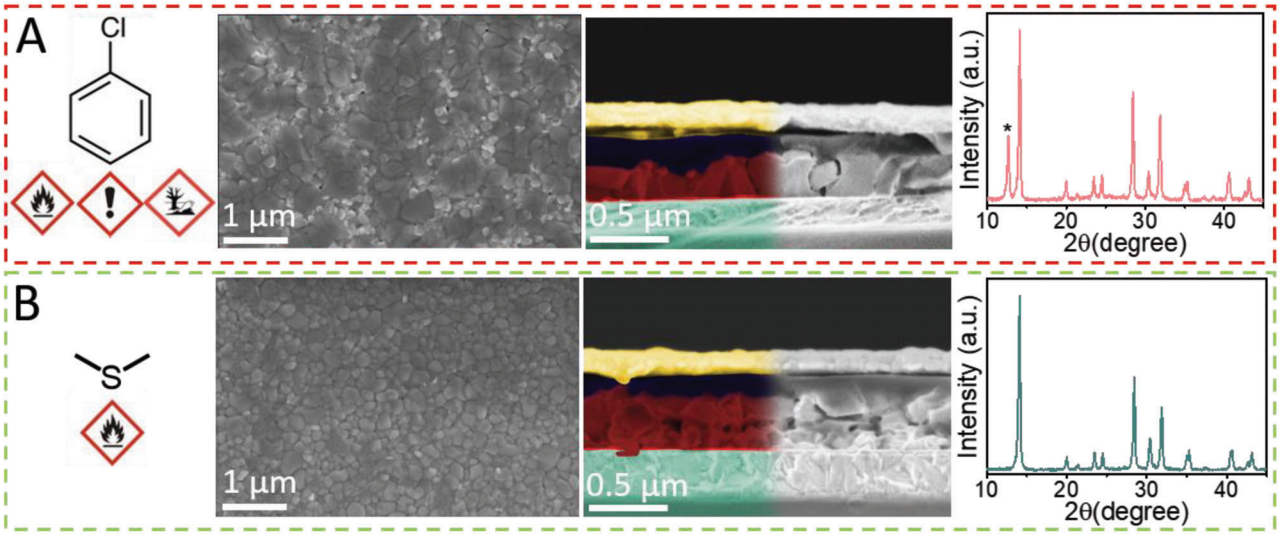

Figure 3. The morphology and crystallinity of $MAPbI_3$ films. A,B) Chemical structures and safety pictograms of CB (A) and DMS (B). While DMS is only flammable, CB poses further health and environmental hazards. Top-view and cross-sectional SEM images, and the XRD pattern of the corresponding perovskite films.

Supporting Information), and a significantly more intense PL-signal, indicating higher crystal quality.

In **Figure 3**, we show the chemical structures and safety information of CB and DMS. CB is a halogenated solvent with flammable, skin/eye irritation and highly toxic properties, which is detrimental to human health and the environment.[37] On the other hand, DMS raises fewer safety concerns, although it has a flammability tendency that needs to be handled with appropriate precautions. DMS is even used as a food additive at low concentrations.[38,39] High-resolution scanning electron microscopy (SEM) and X-ray diffraction (XRD) are used to characterize the morphology and crystallinity of the deposited perovskite films. Both cases provide fully formed perovskite films with almost identical thicknesses; while the film deposited without solvent extraction shows a nonuniform coverage with elongated needle-shaped regions (see Figure S6, Supporting Information).

Previous research explored DE,[40,41] and ethyl acetate (EA) as green solvents with various polarities and functional groups.[42] The authors show that, due to the higher vapor pressure of DE at 58.9 kPa and EA at 9.69 kPa compared to CB at 1.17 kPa at 20 °C, the resulting perovskite films exhibit various nonuniformities.[13,41,43] Interestingly, when we deposit perovskite films by the DMS coordination solvent with an almost similar vapor pressure to DE (58.9 to 53.7 kPa, respectively) (see Table S2, Supporting Information), it still results in a compact and homogeneous morphology comparable to CB and other sulfide-based solvents (Figure S7, Supporting Information). This occurs because the functional group of the solvents appears to play an important role in an improved perovskite crystallization.[44]

Almost all the sulfide-based solvents have the same functional group, i.e., sulfur, and result in reasonable perovskite films (Figure S8 and Table S3, Supporting Information). The perovskite film deposited by DMS presents smaller grain sizes compared to CB, but with much better monodispersity (Figure 3). It has been demonstrated that the morphology and grain size of perovskite films also depends on the extraction of the precursor solvents, the vapor pressures,[17] and processing temperature.[45] As shown in Figure S9 (Supporting Information), the vapor pressure of sulfide-based solvents decreases gradually by decreasing the alkyl chain from DPS to DMS, leading to different evaporation rates during the annealing step, which could be the reason for the different grain sizes. In Note S2 (Supporting Information), we provide a more detailed rationale for the solvent selection and proceed for reasons of conciseness with a mechanism discussion next.

The XRD pattern reveals a pronounced PbI_2 peak at 12.7° for CB, indicating incomplete perovskite crystallization (the PbI_2 peak is assigned with a star in Figure 3). On the other hand, this peak is absent for DMS, indicating a completed reaction of PbI_2 with the organic cation in the presence of DMS. However, the PbI_2 peak is still present for DES and DPS with lower intensity than the CB case (Figure S7, Supporting Information).

The surface elemental analysis and PL spectroscopy of fabricated $MAPbI_3$ films demonstrate significant film quality improvement by the action of the DMS coordination solvent (see Note S2, Supporting Information). The X-ray photoelectron spectroscopy (XPS) data show that the amount of Pb^0 is minimized in the DMS film, indicating negligible surface recombination compared to other cases (Figure S10A,B, Supporting Information). The PL data also present the lowest defect density among all the films for the perovskite film fabricated by DMS (Figure S10C,D, Supporting Information).

Finally, we fabricate PSCs in a typical stack of ITO/SnO_2/perovskite/2,2′,7,7′-tetrakis(*N*,*N*-di-*p*-methoxyphenylamine)–9,9′-spirobifluorene (Spiro-OMeTAD)/gold (see **Figure 4**A and fabrication details can be found in Supporting Information). Previously, we used anisole as a green solvent for Spiro-OMeTAD instead of CB.[46] By avoiding DMF, we can process our devices with a fully green solvent system using water,[47] DMSO,[48] and anisole[46,49] for SnO_2, perovskite

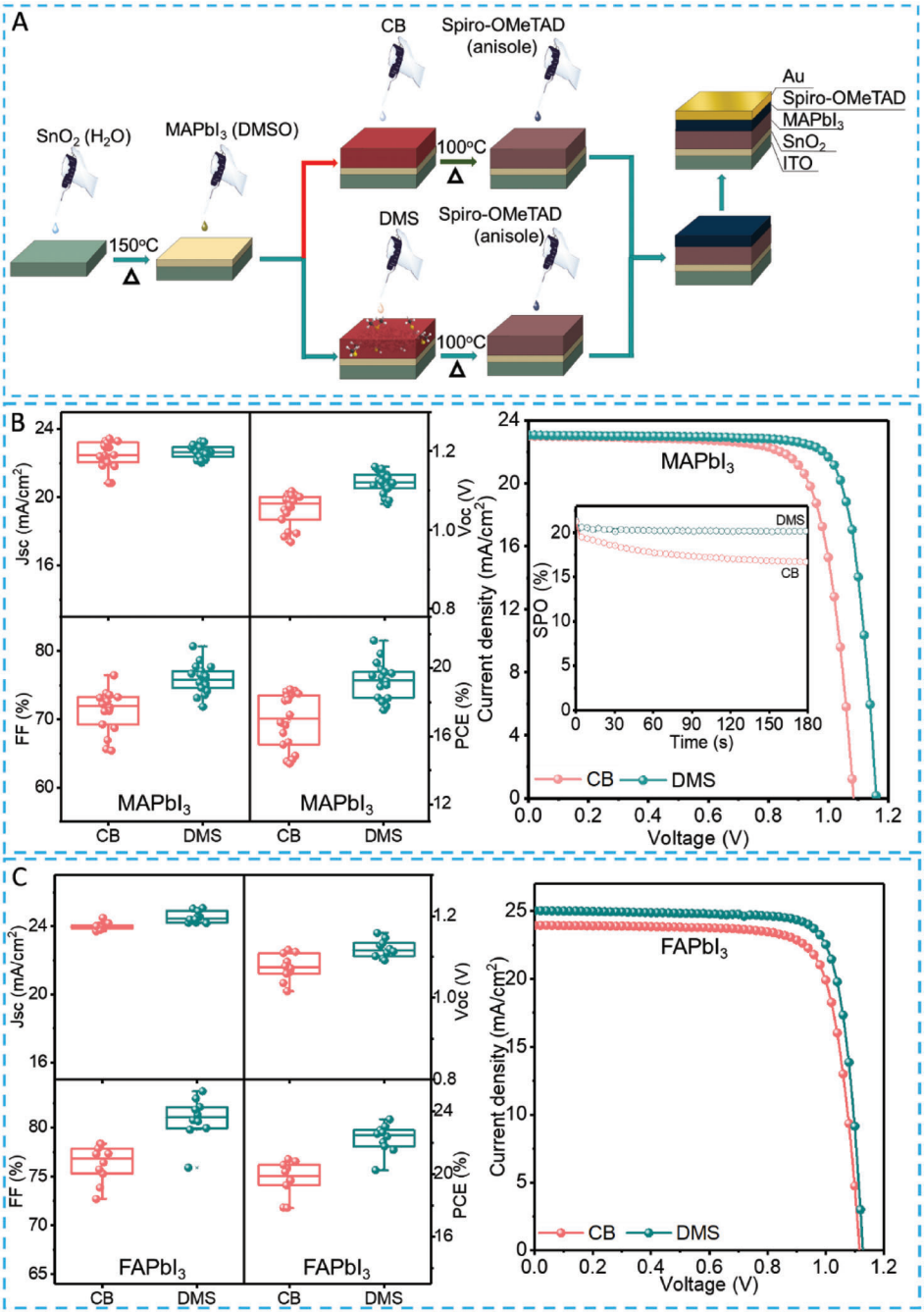

Figure 4. The fabrication process and characterization of PSCs. A) Schematic illustration of PSC processing by non-green (top) and fully green solvents (bottom). B) Statistical photovoltaic parameters and champion *J–V* curves of fabricated PSCs of $MAPbI_3$ by CB and DMS (the inset shows the SPO at the maximum power point voltage for 180 s). C) Performance comparison of $FAPbI_3$-based solar cells using DMS and CB as antisolvents, and comparison of *J–V* curves for champion cells.

precursors, Spiro-OMeTAD, and using DMS for DMSO extraction from the perovskite precursor (see the non-green in Figure S13, Supporting Information and fully green processing paths in Figure 4A).

The statistical photovoltaic parameters, including short-circuit current density (J_{SC}), open-circuit voltage (V_{OC}), fill factor (FF), and PCE for 18 devices, measured in the reverse scan direction for CB and DMS are seen in Figure 4B. The PSCs fabricated by CB present lower photovoltaic parameters than the DMS devices, possibly due to the lower perovskite film quality. Especially V_{OC} and FF are significantly increased in the case of DMS, achieving the higher PCEs with high reproducibility. The PSCs fabricated with the other solvents, i.e., DPS, DES, presented reduced photovoltaic performance compared to DMS (see Figure S14, Supporting Information). In a similar trend, the PSCs using DMS showed negligible hysteresis (Figure S15, Supporting

Table 1. Summary of the photovoltaic parameters obtained from the champion devices for $MAPbI_3$ and $FAPbI_3$ fabricated by CB and DMS. Measurements were performed under AM 1.5G solar illumination.

Composition[a)]		V_{OC} [V]	J_{SC} [mA/cm2]	FF	PCE [%]
$MAPbI_3$	CB	1.09	23.0	0.76	19.1
	DMS	1.16	23.0	0.81	21.6
$FAPbI_3$	CB	1.12	23.9	0.78	20.9
	DMS	1.12	25.1	0.84	23.5

[a)] Cell size: 0.16 cm^2. A shadow mask was used to define the active area.

Information) indicating the dependence of device performance on film quality.[50]

Figure 4B and **Table 1** compare the champion current–voltage (*J–V*) characteristics of PSCs fabricated using CB and DMS. A substantial performance improvement from 19.1% for CB to 21.6% for DMS is observed, mainly due to improved V_{OC} from 1.09 to 1.16 V and FF from 0.76 to 0.81. This PCE of 21.6% is among the highest reported value for fully green solvent-processed n–i–p $MAPbI_3$ PSCs (see Table S4 and Note S3, Supporting Information).

The improved V_{OC} and FF of PSCs fabricated by DMS are attributed to the efficient crystallization and defect passivation of the perovskite films. To prove this concept, the ideality factor is determined by measuring the V_{OC} dependence on the light intensity (see characterization methods in Supporting Information). As shown in Figure S17 (Supporting Information), the value of the ideality factor decreases significantly from 1.93 for the devices fabricated by CB to 1.27 for the DMS ones. This result is an indication of reduced surface defects at the perovskite/HTL interface. Additionally, we measure the stabilized power output (SPO) at a fixed maximum power point voltage over time to better understand our photovoltaic observations (Figure 4B inset). The PSC fabricated by DMS presents a stabilized PCE of ≈20.7% for 180 s, which is very close to the original PCE from the *J–V* curve. In contrast, in the case of CB, the SPO decreases over time (stabilized PCE of ≈16.7%), which confirms the lower quality of perovskite film causing the high *J–V* hysteresis. Moreover, the PSC fabricated by DMS shows a lower dark current than the CB sample, suggesting a lower dark leakage current due to improved charge transport and decreased recombination loss in the device (See Figure S18, Supporting Information). The *J–V* curves of the champion cells for all samples are shown in Figure S19 (Supporting Information), and detailed performance parameters are shown in Table S5 (Supporting Information).

As shown in Figure S20 (Supporting Information), the integrated current densities of ≈22.3 mA cm^{-2} and ≈22.3 mA cm^{-2} calculated from the external quantum efficiency (*EQE*) spectra of CB and DMS champion devices agree with the current densities of the *J–V* measurement. We also performed a 16-days performance data tracking measurement on 9 devices, and the results showed that the DMS-based solar cells were more stable, which might be due to the passivated defects in the corresponding perovskite films. In contrast, the variance of the performance parameters of the CB solar cells shown in the box charts is bigger (see Figures S21 and S22, Supporting Information).

To prove the universality of our strategy, we fabricated $FAPbI_3$ perovskite solar cells by means of CB and DMS. As shown in Figure 4c, similar to $MAPbI_3$ composition, the mean values of V_{oc} and FF for fabricated $FAPbI_3$ solar cells with DMS is significantly increased compared to CB counterpart. These data demonstrate that even though the fabrication strategies (excluding the antisolvent process) for $FAPbI_3$ and $MAPbI_3$ cells differ, the films fabricated using DMS as an coordination solvent show similar improvements in device performance when compared to the control group. Moreover, as shown in Table 1, the $FAPbI_3$ champion device with DMS exhibits a high efficiency of 23.5% with a FF of 0.84, while the fabricated solar cell with CB performs only at 20.9% PCE with 0.78 FF.

3. Conclusion

Currently, DMF-rich solvent systems are used to dissolve the precursor components of practically all high-performance perovskite solar cells. Unfortunately, DMF hydrolyses and is therefore a long-term risk to stability. One pathway to avoid DMF is the usage of pure DMSO, but this is not an option for the state-of-the-art multicomponent perovskites. Interestingly, the now less prominent $MAPbI_3$ perovskite requires pure DMSO but could never reach performances >21% due to the challenging extraction of the DMSO molecules which form complexes with Pb^{2+}.

Many other reports have reported on "better" antisolvents than CB based on the rationale of supersaturating the perovskite precursor. Instead, here we introduce a novel (and green) solvent, DMS, based on the rationale of strong coordination chemistry for extracting the DMSO from the perovskite precursor efficiently and promote a controllabled crystallization. The results show that DMS assists to form the intermediate phase in a short time due to its high Gutmann donor number. This leads to a higher quality perovskite layer than the other similar solvents due its high vapor pressure so that the annealing temperature is well below the degradation temperature of the perovskite. Consequently, in line with industry needs, we show that our novel solvent system can be used as the basis to process all layers, including electron-transporting layer, perovskite, and hole-transporting layer, with green solvents. The fully green-solvent-processed $MAPbI_3$ PSC delivered a champion efficiency of 21.6% and 23.5% for $FAPbI_3$, demonstrating superior performance compared to the control devices.

4. Experimental Section

Materials: The chemicals and solvents were obtained commercially and used without further purification. SnO_2 colloid precursor (15% in H_2O colloidal dispersion) was purchased from Alfa Aesar. The organic cation halide salts for perovskite methylammonium iodide (MAI) were purchased from Greatcell Solar Materials. PbI_2 was purchased from TCI. Spiro-OMeTAD (99.5%), 4-Tert-butyl pyridine (99.9%), lithium bis(trifluoromethylsulphonyl) imide (99.95%), and FK209 Co(III) TFSI salt (98%) were purchased from Advanced Election Technology Co., Ltd., TCI, Sigma-Aldrich, and Dyesol, respectively. All solvents, including dimethylformamide (DMF), dimethyl sulfoxide (DMSO), chlorobenzene (CB), dimethyl sulfide (DMS), diethyl sulfide (DES), and dipropyl sulfide (DPS), anisole (ANS), and acetonitrile (ACN) were purchased from Sigma-Aldrich.

Device Fabrication: For $MAPbI_3$, patterned indium-tin oxide (ITO) substrates (7 Ω/sq, AGC) were ultrasonically cleaned with 2% Hellmanex water solution, deionized (DI) water, acetone, and isopropanol (IPA). Before use, the as-cleaned substrates were further cleaned with UV–ozone treatment for 15 min. Then the SnO_2 solution (2.67%, diluted by water) was spin-coated onto the substrates at 3000 rpm for 25 s and annealed on a hot plate at 150 °C for 30 min under an ambient atmosphere. After cooling down to room temperature, the substrates were treated with UV–ozone for 20 min. The perovskite precursor solution was prepared with 1.3 M $MAPbI_3$ in anhydrous DMSO. Then the perovskite precursor solution was spin-coated onto SnO_2 with a two-step program at 1000 and 6000 rpm for 5 and 27 s, respectively, in a nitrogen-filled glovebox. During the spin-coating process, different cases such as CB, DPS, DES, and DMS were dripped on the spinning substrate slowly for 5 s before the end of the program, followed by annealing at 100 °C for 60 min. After cooling down to room temperature, the spiro-OMeTAD solution (73.2 mg in 1 mL CB) doped with 18 µL of Li-TFSI (520 mg mL^{-1} in ACN), 29 µL of FK209 Co (III) TFSI salt (300 mg mL^{-1} in ACN), and 29 µL tBP was coated at 4000 rpm for 30 s. Finally, 100 nm of gold was thermally evaporated under a pressure of 10^{-6} mbar as the back electrode.

For $FAPbI_3$, the fluorine-doped tin oxide (FTO) glasses were cleaned with detergent, DI water, acetone, and IPA using an ultrasonic bath for 20 min as a sequential process. The FTO substrates were treated by UV–ozone cleaner for 15 min before depositing the compact titanium dioxide (c-TiO_2). The c-TiO_2 film was deposited on the FTO substrates using spray pyrolysis method with 0.4 mL of acetylacetone, 0.6 mL of titanium diisopropoxide bis(acetylacetonate in 9 mL of ethanol. This deposition process was implemented in situ annealing for an hour on a 450 °C of a hotplate. The UV–ozone treatment was conducted for the FTO/c-TiO_2 substrates were cooled down for 15 min. The mesoporous titanium dioxide (mp-TiO_2) solution was prepared as following the recipe that 150 mg of TiO_2 paste was diluted in 1 mL of ethanol solvent. The mp-TiO_2 film was implemented by spin-coating method at 4000 rpm for 30 s. The mp-TiO_2 film deposited FTO/c-TiO_2 substrates were annealed to 450 °C at ambient air condition. The perovskite precursor was prepared 9% of Pb excess with 1.25 M concentration in the stoichiometry of $FAPbI_3$ plus 40 mol% of methylammonium chloride in DMF: DMSO with 8.5:1 of the volume ratio. Before deposition of the perovskite absorber layer, the FTO/c-TiO_2/mp-TiO_2 substrates were treated by UV–ozone cleaner for 15 min again. From perovskite film to spiro-MeOTAD layer were implemented in the glove box. The spin-coating program for the perovskite layer is a two-step spin coating method where the first step is 1000 rpm for 10 s and the second step is 5000 rpm for 20 s. During the second step of the spin-coating program, the coordinated solvent treatment was performed with CB and DMS one another. The FTO/c-TiO_2/mp-TiO_2/perovskite substrates were annealed for 10 min on the hotplate at 150 °C. After finishing the produce of the perovskite film, n-octylammonium iodide (OAI) passivation layer was deposited that OAI solution is made up of 5 mg of OAI in 1 mL of IPA with spin coating. The parameter is 4000 rpm for 30 s and the substrates were annealed for a short time at 100 °C. The spiro-OMeTAD and gold layers were deposited by the same recipe as used for $MAPbI_3$ devices.

Characterization: For X-ray photoelectron spectroscopy (XPS) and ultraviolet photoelectron spectroscopy (UPS), the perovskite layer prepared with various solvent treatments is analyzed with X-ray photoelectron spectroscopy using Al k-Alpha source (1486.5 eV) non-monochromitized X-ray. The photoelectrons are collected with the hemispherical analyzer from PHOIBOS HSA3500. The photoemitted electrons were collected at a right angle to the surface of the sample. The detailed spectra of each element present on the samples are collected with a pass energy of 20 eV and a scan rate of 0.1 eV. The collected spectra were analyzed with the Casa XPS software, and the peaks were fitted with a mixed Gaussian-Lorentzian line shape with a Shirley background. The binding energy of the measured spectra is corrected with respect to the metallic Pb (137.00 eV) and advantageous carbon (285. 00 eV). FT-IR spectra were recorded from the neat powder of the respective analyte on a BRUKER JASCO FT-IR-4100 spectrometer. An Ocean Optics spectrometer (Flame) coupled with fiber optics was used to acquire transmission measurements with an integration time of ≈0.15 s (spin-coating) to 0.4 s (annealing) per transmission spectrum and a wavelength spacing of ≈1.3 nm in an N_2-filled glove box. The equation $[A_\lambda = -\log 10(T_\lambda)]$ was used to calculate the UV–vis absorption spectra from the transmission spectra, where A_λ is the absorbance at a certain wavelength (λ), and T_λ is the corresponding transmitted radiation. The in situ UV–vis transmission/absorption measurements during spin-coating were performed using a setup. The in situ UV–vis transmission/absorption measurements during thermal annealing were performed using a custom-built heating stage with a hole that allows analog transmission. The in situ PL measurements were carried out using a home-built setup in an N_2-filled glove box. Excitation was performed using a laser diode emitting at 405 nm and the PL emission was collected using an optical fiber coupled with an Ocean Optics spectrometer (Flame). A Jacobian correction was applied to the data transforming them from wavelength- to energy-space and fitting them using a Gaussian and a constant background. Integration times of 300 ms were used. The GIWAXS data were collected at the 12.3.2 microdiffraction beamline of the Advanced Light Source (ALS) in a custom-made analytical spin-coater allowing for simultaneous film-deposition and diffraction measurements. The SEM images were acquired in a Zeiss Crossbeam 550 system at low beam energies (5 kV 69 pA for the topview images and 2 kV 41 pA for the cross-sections). The cross-section samples were mechanically cleaved with a glass-breaking tool. No conductive coatings were applied. For the steady-state PL, we used an Andor Kymera 193i spectrometer illuminated at 422 nm @ ≈3 sun for 1 s. For the time-resolved photoluminescence (TRPL) the illumination was made at 510 nm @ ≈1 sun, with a stopping condition of 1×10^3 counts. The spectrometer was centered at either 760 or 770 nm with a bandwidth of 40 nm. It was run on a Lifespec 2, with a 5 nJ cm^{-2} fluence. Nevertheless, PL and TRPL analysis was performed using Thot data management and analysis software.

Supporting Information

Supporting Information is available from the Wiley Online Library or from the author.

Acknowledgements

M.S. thanks the German Research Foundation (DFG) for funding (SPP2196, 431314977/GRK 2642). M.S. acknowledges funding from the European Research Council under the Horizon program (LOCAL-HEAT, grant agreement no. 101041809). M.S. acknowledges funding from the German Bundesministerium für Bildung and Forschung (BMBF), project "NETPEC" (01LS2103E). M.S. acknowledges funding by ProperPhotoMile. Project ProperPhotoMile is supported under the umbrella of SOLAR-ERA.NET Cofund 2 by The Spanish Ministry of Science and Education and the AEI under the project PCI2020-112185 and CDTI project number IDI-20210171; the Federal Ministry for Economic Affairs and Energy on the basis of a decision by the German Bundestag project number FKZ 03EE1070B and FKZ 03EE1070A and the Israel Ministry of Energy with project number 220-11-031. SOLAR-ERA.NET is supported by the European Commission within the EU Framework Programme for Research and Innovation HORIZON 2020 (Cofund ERA-NET Action, No. 786483). Furthermore, T.K. thanks the German Research Foundation (DFG) for funding (KO6414). This research used Beamline 12.3.2, supported by Nobumichi Tamura, which is a resource of the Advanced Light Source, a U.S. DOE Office of Science User Facility under contract no. DE-AC02-05CH11231. In situ characterizations at the Molecular Foundry were supported by the Office of Science, Office of Basic Energy Sciences, of the U.S. Department of Energy under Contract No. DE-AC02-05CH11231. The authors thank Simon Briesenick and Meredith Goudreau for their assistance in carrying out the in situ characterization.

Open access funding enabled and organized by Projekt DEAL.

Conflict of Interest

The authors declare no conflict of interest.

Data Availability Statement

The data that support the findings of this study are available from the corresponding author upon reasonable request.

Keywords

coordination chemistry, green solvents, perovskite crystallization

Received: March 29, 2023
Revised: May 26, 2023
Published online: August 9, 2023

[1] A. Kojima, K. Teshima, Y. Shirai, T. Miyasaka, *J. Am. Chem. Soc.* **2009**, *131*, 6050.
[2] J. Park, J. Kim, H.-S. Yun, M. J. Paik, E. Noh, H. J. Mun, M. G. Kim, T. J. Shin, S. I. Seok, *Nature* **2023**, *616*, 724.
[3] Z. Yao, W. Zhao, S. Liu, *J. Mater. Chem. A* **2021**, *9*, 11124.
[4] R. Jono, H. Segawa, *Chem. Lett.* **2019**, *48*, 877.
[5] S. Masi, A. F. Gualdrón-Reyes, I. Mora-Seró, *ACS Energy Lett.* **2020**, *5*, 1974.
[6] M. Saliba, T. Matsui, J.-Y. Seo, K. Domanski, J.-P. Correa-Baena, M. Khaja, S. M. Zakeeruddin, W. Tress, A. Abate, A. Hagfeldt, M. Grätzel, *Energy Environ. Sci.* **2016**, *9*, 1989.
[7] B. Conings, J. Drijkoningen, N. Gauquelin, A. Babayigit, A. Ethirajan, J. Verbeeck, J. Manca, E. Mosconi, F. de Angelis, H.-G. Boyen, B. Conings, J. Drijkoningen, A. Babayigit, A. Ethirajan, H. Boyen, N. Gauquelin, J. Verbeeck, E. Mosconi, F. de Angelis, *Adv. Energy Mater.* **2015**, *5*, 1500477.
[8] N. J. Jeon, J. H. Noh, Y. C. Kim, W. S. Yang, S. Ryu, S. I. Seok, *Nat. Mater.* **2014**, *13*, 897.
[9] Y.-J. Kang, S.-N. Kwon, S.-P. Cho, Y.-H. Seo, M.-J. Choi, S.-S. Kim, S.-I. Na, *ACS Energy Lett.* **2020**, *5*, 2535.
[10] Y. Wang, J. Wu, P. Zhang, D. Liu, T. Zhang, L. Ji, X. Gu, Z. D. Chen, S. Li, *Nano Energy* **2017**, *39*, 616.
[11] A. D. Taylor, Q. Sun, K. P. Goetz, Q. An, T. Schramm, Y. Hofstetter, M. Litterst, F. Paulus, Y. Vaynzof, *Nat. Commun.* **2021**, *12*, 1878.
[12] D.-K. Lee, K.-S. Lim, J.-W. Lee, N.-G. Park, *J. Mater. Chem. A* **2021**, *9*, 3018.
[13] S. Paek, P. Schouwink, E. N. Athanasopoulou, K. T. Cho, G. Grancini, Y. Lee, Y. Zhang, F. Stellacci, M. K. Nazeeruddin, P. Gao, *Chem. Mater.* **2017**, *29*, 3490.
[14] K. M. Lee, C. J. Lin, B. Y. Liou, S. M. Yu, C. C. Hsu, V. Suryanarayanan, M. C. Wu, *Sol. Energy Mater. Sol. Cells* **2017**, *172*, 368.
[15] T. Moot, A. R. Marshall, L. M. Wheeler, S. N. Habisreutinger, T. H. Schloemer, C. C. Boyd, D. R. Dikova, G. F. Pach, A. Hazarika, M. D. McGehee, H. J. Snaith, J. M. Luther, *Adv. Energy Mater.* **2020**, 10, 1903365.
[16] E. J. Cassella, E. L. K. Spooner, J. A. Smith, T. Thornber, M. E. O'Kane, R. D. J. Oliver, T. E. Catley, S. Choudhary, C. J. Wood, D. B. Hammond, H. J. Snaith, D. G. Lidzey, *Adv. Energy Mater.* **2023**, *13*, 2203468.
[17] S. G. Kim, J. H. Kim, P. Ramming, Y. Zhong, K. Schötz, S. J. Kwon, S. Huettner, F. Panzer, N. G. Park, *Nat. Commun.* **2021**, *12*, 1554.
[18] V. Gutmann, *Coord. Chem. Rev.* **1976**, *18*, 225.
[19] F. Arnaud-Neu, R. Delgado, S. Chaves, Critical Evaluation of Stability Constants and Thermodynamic Functions of Metal Complexes of Crown Ethers (IUPAC Technical Report), Brazil **2003**.
[20] J. C. Hamill, J. Schwartz, Y.-L. Loo, ACS Energy Lett. **2018**, *3*, 49.
[21] X. Huang, G. Deng, S. Zhan, F. Cao, F. Cheng, J. Yin, J. Li, B. Wu, N. Zheng, *ACS Cent. Sci.* **2022**, *8*, 1008.
[22] C. F. Zheng, H. Takenaka, F. Wang, N. Z. Koocher, A. M. Rappe, *J. Phys. Chem. Lett.* **2015**, *6*, 50.
[23] G. R. Berdiyorov, F. El-Mellouhi, M. E. Madjet, F. H. Alharbi, S. N. Rashkeev, *Appl. Phys. Lett.* **2016**, 108, 053901.
[24] G. R. Berdiyorov, F. El-Mellouhi, M. E. Madjet, F. H. Alharbi, F. M. Peeters, S. Kais, *Sol. Energy Mater. Sol. Cells* **2016**, *148*, 2.
[25] G. R. Berdiyorov, M. E. Madjet, F. El-Mellouhi, F. M. Peeters, *Sol. Energy Mater. Sol. Cells* **2016**, *148*, 60.
[26] F. Bella, G. Griffini, J. P. Correa-Baena, G. Saracco, M. Grätzel, A. Hagfeldt, S. Turri, C. Gerbaldi, *Science (1979)* **2016**, *354*, 203.
[27] H. Turren-Cruz, A. Hagfeldt, M. Saliba, *Science* **2018**, *362*, 449.
[28] L. Shi, M. P. Bucknall, T. L. Young, M. Zhang, L. Hu, J. Bing, D. S. Lee, J. Kim, T. Wu, N. Takamure, D. R. McKenzie, S. Huang, M. A. Green, A. W. Y. Ho-Baillie, *Science* **2020**, *368*, 1328.
[29] P. Holzhey, P. Yadav, S. H. Turren-Cruz, A. Ummadisingu, M. Grätzel, A. Hagfeldt, M. Saliba, *Mater. Today* **2019**, *29*, 10.
[30] N.-K. Kim, Y. H. Min, S. Noh, E. Cho, G. Jeong, M. Joo, S.-W. Ahn, J. S. Lee, S. Kim, K. Ihm, H. Ahn, Y. Kang, H.-S. Lee, D. Kim, *Sci. Rep.* **2017**, *7*, 4645.
[31] I. Barnes, K. H. Becker, I. Patroescu, *Atmos. Environ.* **1996**, *30*, 1805.
[32] A. A. Petrov, S. A. Fateev, V. N. Khrustalev, Y. Li, P. v Dorovatovskii, Y. v Zubavichus, E. A. Goodilin, A. B. Tarasov, *Chem. Mater.* **2020**, *32*, 7739.
[33] S. Pratap, F. Babbe, N. S. Barchi, Z. Yuan, T. Luong, Z. Haber, T.-B. Song, J. L. Slack, C. v Stan, N. Tamura, C. M. Sutter-Fella, P. Müller-Buschbaum, *Nat. Commun.* **2021**, *12*, 5624.
[34] J. Li, A. Dobrovolsky, A. Merdasa, E. L. Unger, I. G. Scheblykin, *ACS Omega* **2018**, *3*, 14494.
[35] S. Kim, H. Oh, G. Kang, I. K. Han, I. Jeong, M. Park, *ACS Appl. Energy Mater.* **2020**, *3*, 6995.
[36] J. Li, X. Yuan, P. Jing, J. Li, M. Wei, J. Hua, J. Zhao, L. Tian, *RSC Adv.* **2016**, *6*, 78311.
[37] N. G. Park, *Nat. Sustainability* **2021**, *4*, 192.
[38] R. Hanif, L. Qiao, S. J. Shiff, B. Rigas, *J. Lab. Clin. Med.* **1997**, *130*, 576.
[39] T. H. Parliment, M. G. Kolor, I. Y. Maing, *J. Food Sci.* **1977**, *42*, 1592.
[40] F. P. Byrne, S. Jin, G. Paggiola, T. H. M. Petchey, J. H. Clark, T. J. Farmer, A. J. Hunt, C. R. Mcelroy, J. Sherwood, *Sustainable Chem. Processes* **2016**, *4*, 7.
[41] Y. Cui, S. Wang, L. Ding, F. Hao, *Adv. Energy Sustainability Res.* **2021**, *2*, 2000047.
[42] T. Bu, X. Liu, Y. Zhou, J. Yi, X. Huang, L. Luo, J. Xiao, Z. Ku, Y. Peng, F. Huang, Y.-B. Cheng, J. Zhong, *Energy Environ. Sci* **2017**, *10*, 2509.
[43] H. Beng Lee, M.-K. Jeon, N. Kumar, B. Tyagi, J.-W. Kang, H. B. Lee, M. Jeon, N. Kumar, B. Tyagi, J. Kang, *Adv. Funct. Mater.* **2019**, *29*, 1903213.
[44] J. W. Lee, H. S. Kim, N. G. Park, *Acc. Chem. Res.* **2016**, *49*, 311.
[45] H. Taherianfard, G. W. Kim, M. M. Byranvand, K. Choi, G. Kang, H. Choi, F. Tajabadi, N. Taghavinia, T. Park, *ACS Appl. Energy Mater.* **2020**, *3*, 1506.
[46] M. Yavari, M. Mazloum-Ardakani, S. Gholipour, M. Mahdi Tavakoli, S.-H. Turren-Cruz, N. Taghavinia, M. Grätzel, A. Hagfeldt, M. Saliba, G. M. Solvents Yavari, S. Turren-Cruz, A. Hagfeldt, M. Yavari, M. Mazloum-Ardakani, S. Gholipour, M. M. Tavakoli, M. Grätzel, A. San Claudio, S. Col San Manuel, M. Saliba, *Adv. Energy Mater.* **2018**, *8*, 1800177.
[47] Q. Jiang, Y. Zhao, X. Zhang, X. Yang, Y. Chen, Z. Chu, Q. Ye, X. Li, Z. Yin, J. You, *Nat. Photonics* **2019**, *13*, 460.
[48] J. Küffner, J. Hanisch, T. Wahl, J. Zillner, E. Ahlswede, M. Powalla, *ACS Appl. Energy Mater.* **2021**, *4*, 11700.
[49] J. Lee, M. Malekshahi Byranvand, G. Kang, S. Y. Son, S. Song, G.-W. Kim, T. Park, *J. Am. Chem. Soc.* **2017**, *139*, 12175.
[50] H. J. Snaith, A. Abate, J. M. Ball, G. E. Eperon, T. Leijtens, N. K. Noel, S. D. Stranks, J. Tse, W. Wang, K. Wojciechowski, W. Zhang, *J. Phys. Chem. Lett* **2014**, *5*, 1511.